J. Fluid Mech. (2026), *vol.* 1027, A30, doi:10.1017/jfm.2025.11002

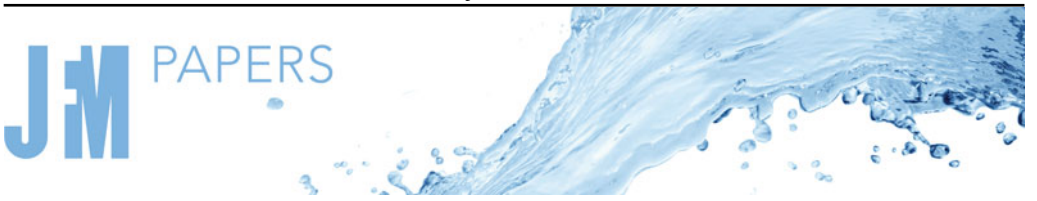

Elastically encapsulated core annular flow

Thomasina V. Ball[1], **Neil J. Balmforth**[2], **Sean Delfel**[3], **Jordan MacKenzie**[3] **and D. Mark Martinez**[4]

[1]Mathematics Institute, University of Warwick, Coventry CV4 7AL, UK

[2]Department of Mathematics, University of British Columbia, Vancouver, BC V6T 1Z2, Canada

[3]Northiana Energy Solutions, 9123 Bentley St, Vancouver, BC V6P 6G2, Canada

[4]Department of Chemical and Biological Engineering, University of British Columbia, Vancouver, BC V6T 1Z2, Canada

Corresponding author: Thomasina V. Ball, thomasina.ball@warwick.ac.uk

(Received 17 June 2025; revised 3 October 2025; accepted 20 November 2025)

We present a combined experimental and theoretical exploration of three-layer, horizontal core–annular pipe flow, in which two fluids are separated by a deformable elastic solid. In the experiments, an elastic solid created by an *in situ* chemical reaction maintains the separation of the core and annular fluids. Corrugations of the elastic interface are observed, and stable pipelining, where the elastic shell created separating the two fluids remains intact, is successfully demonstrated even when the core fluid is buoyant. The theoretical model combines lubrication theory for the fluids with standard shell theory for the elastic solid. The model is used to predict the buckling states resulting from radial compression of the shell, and to explore the sedimentation of a buoyant core. The self-sculpting of the shell by buckling cannot by itself generate hydrodynamic lift owing to symmetry in the direction of flow. Instead, we demonstrate that hydrodynamic lift can be achieved by other elastohydrodynamic effects, when that symmetry becomes broken during the bending of the shell.

Key words: lubrication theory, instability, drag reduction

1. Introduction

Core–annular flows are often proposed to reduce frictional losses in industrial pipeline transport processes (e.g. Charles, Govier & Hodgson 1961; Joseph *et al.* 1997; Joseph & Renardy 2013*a*,*b*). In conventional two-layer flows, a low-viscosity lubricating film is placed around a more viscous core to reduce the drag on the core. This configuration

is, however, prone to a wide variety of undesired flow instabilities and regimes, as documented by Joseph *et al.* (1997), McKibben, Gillies & Shook (2000), Bannwart *et al.* (2004), Sotgia, Tartarini & Stalio (2008), Ghosh *et al.* (2009), Rodriguez, Bannwart & De Carvalho (2009), Sun *et al.* (2022) and Xie *et al.* (2023). These studies collectively suggest that while friction reduction is achievable in principle, maintaining core–annular flow remains a significant challenge, which perhaps rationalises the lack of a widespread adoption of core–annular fluid lubrication in industrial practices.

A further difficulty with horizontal pipelines is the density difference that is invariably present between the core and the lubricating fluid. With buoyancy, the core migrates vertically under such differences, potentially interrupting the lubrication process. Nevertheless, Ooms and co-workers (Ooms & Beckers 1972; Ooms & Poesio 2003; Ooms *et al.* 2007, 2013) have suggested that sufficiently permanent, asymmetrical corrugations or other deformations of the interface between the two fluids can generate hydrodynamic lift forces that may counter gravity.

The issues with conventional two-fluid core–annular flows prompted Frigaard and co-workers to explore three-fluid configurations, in which an inert intermediate layer separates the lubricating film from the core (e.g. Moyers-Gonzalez, Frigaard & Nouar 2004; Huen, Frigaard & Martinez 2007; Hormozi, Wielage-Burchard & Frigaard 2011; Sarmadi *et al.* 2017, 2018). This configuration offers the possibility of exploiting the material properties of the intervening fluid to stabilise flow instabilities and help to maintain the separation between core and lubricant. In particular, Frigaard and co-workers have suggested using the yield stress of an intervening viscoplastic fluid layer for the task. Moreover, in combination with the hydrodynamic lift generated by unyielded interfacial corrugations, stable pipelining, where the core and lubricant remain separated, might be feasible even with density differences in a horizontal pipeline (Sarmadi *et al.* 2017, 2018). Nevertheless, three-layer core–annular flow with a yield-stress fluid remains relatively novel and largely unexplored.

The present work aims to address the limitations of two-fluid core–annular flow in a related, but different manner: rather than emplacing a yield-stress fluid between core and lubricant, we consider a three-layer arrangement in which an elastic material acts as the buffer, as sketched in figure 1(*b*). The emplacement of a cylindrical elastic shell between core fluid and lubricant might seem difficult to achieve in any practical setting. Moreover, one might consider the final removal and disposal of the buffer material to be an excessively costly component in any pipelining process. However, recent work with hydrogels (e.g. sodium alginate) have shown that an elastic shell can be generated and emplaced relatively effectively by *in situ* chemical reaction with polyvalent ionic solutions as shown in figure 1(*a*) (MacKenzie *et al.* 2022); the gel and its constituent reactants are relatively inexpensive and disposable.

In the current paper, we continue in this vein, and begin by presenting a series of experiments exploring core–annular flows with an elastic buffer (§ 2). We provide evidence for the viability of the configuration for stable pipelining at high Reynolds number, showing that the elastic layer effectively isolates the core fluid, preventing mixing even in the presence of large density contrasts. The shell also maintains the core away from the edge of the pipe, suggesting the presence of some form of Ooms's hydrodynamic lift effect to offset buoyancy.

Given the success of this experimental effort, we then continue to the main goal of the present paper: the development of a mathematical model of elastically encapsulated core–annular flow. For this task, we resort to some idealisations that are common in the description of core–annular fluid dynamics and elastic shells: as outlined in § 3, we combine lubrication theory for the outer fluid lubricant with the classical theory of

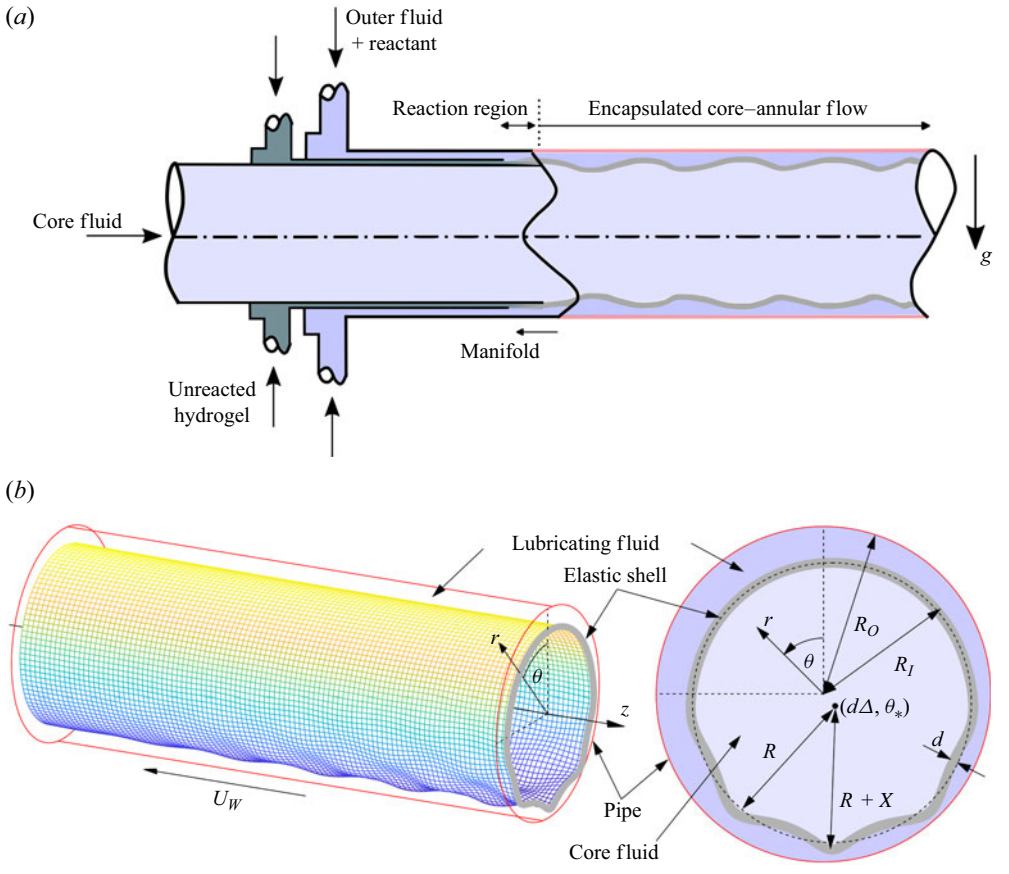

Figure 1. (*a*) Sketch of the experimental set-up. (*b*) Sketch of the model geometry described in § 3. The centroid of the shell relative to the centre of the pipe is given by radial polar coordinates $(d\Delta, \theta_*)$. In the frame of the shell, the pipe wall moves to the left with speed U_W.

cylindrical shells of von Kármán and Donnell (Yamaki 1984) for the elastic encapsulant. Implicitly, the model assumes that both the lubricant and shell have negligible inertia and are relatively thin, so that the core fluid fills most of the pipe and is largely held at hydrostatic pressure without participating to any significant degree in the detailed dynamics. The model does not therefore match the high Reynolds number of the experiments, a discrepancy to which we return in our conclusions.

In the von Kármán–Donnell theory, the elastic shell is sufficiently stiff to effectively resist stretching, but not bending. Consequently, the problem devolves to a fluid–structure interaction problem involving the interplay between core–annular flow and a cylindrical elastic shell. The shell can be placed under compression by changing the pressures in the core and lubricant, allowing for the possibility of a novel type of buckling in which the redistribution of the fluid lubricant controls the growth rate of instability. Alternatively, when the shell is tethered somewhere along the pipe, the gravitational load on the encapsulated core fluid prompts bending further along. In either case, the stage is set for the sculpting of the shell (bends, buckles or other corrugations) to generate the hydrodynamic lift needed for stable pipelining. Our purpose is then to interrogate the dynamics of this fluid–structure interaction, and gauge the competition between lift and gravity.

Having formulated the model, we therefore explore the dynamics of buckling of the shell under pressure loading from the two fluids, and how the encapsulated core fluid settles

Case	Core composition (wt/wt %)	ρ_c (kg m^{-3})	ρ_l (kg m^{-3})	μ_c (mPa s)
A	0.3 % $CaCl_2$	1002	1010	1
B	2 % $CaCl_2$	1010	1010	1
C	4 % $CaCl_2$	1018	1010	1
D	4 % sand + 0.3 % $CaCl_2$	1025	1010	20
E	0.4 % xanthan gum + 12 % sand + 0.3 % $CaCl_2$	1077	1010	150

Table 1. Summary of the fluid densities in the core and lubricant ρ_c, ρ_l , respectively, and the core viscosities μ_c for the five experiments. For the core fluid, we estimate the viscosity based on the pressure drop measured in the pipe for that fluid alone. The viscosity of the outer fluid is close to that of water ($\mu_l \approx 1$ mPa s) for all cases.

under gravity. Both have counterparts in other problems in solid and fluid mechanics. We first provide a general linear stability theory for the buckling of the shell (§ 4). Next, we explore how the shell may fall under gravity and buckle in the simpler situation when there are no axial variations along the pipe (§ 5). We then consider the conspiracy between angular and axial buckling (§ 6), but without gravity. Finally, we explore the lift generated by the elastohydrodynamic lubrication of a falling, but tethered shell (§ 7).

2. Experimental demonstration

To investigate the feasibility of sustained encapsulated core–annular flow, we conduct a series of laboratory experiments in a horizontal, straight, smooth-walled pipe of length 10 m and inner diameter $R_O = 50$ mm. At the inlet, the elastic shell is formed *in situ* using a custom-designed three-dimensional extrusion-printing manifold, following the procedure outlined by MacKenzie *et al.* (2022); see figure 1(*a*). This manifold introduces a calcium chloride solution around the outer periphery of the pipe surrounding a 1 % sodium alginate solution. The two fluids then react as they flow into the pipe, generating a stiff, elastic shell. Once the alginate is fully reacted, the remaining calcium chloride solution serves as the outer lubricant. All three layers (the outer lubricating solution, the intervening shell, and the core) are conveyed further down the pipe by an imposed pressure drop.

Independent flow control in the core and annular regions is achieved via variable-frequency-regulated positive-displacement pumps, each drawing fluid from a 500 l feed reservoir. A total volumetric flux of $Q \approx 44$ l min^{-1} is achieved, as measured using a Rosemount 8711 electromagnetic flowmeter. For water, this flux corresponds to Reynolds number approximately $Re = 2300$, based on a 6.25 mm annular gap; lower Reynolds number flow was not achievable in this flow set-up.

The pressure drop was measured across a 1 m section of the pipe using a Rosemount 1151DP differential pressure transducer. Five distinct flow configurations were explored, with a variety of density differences between the core fluid and lubricant, ranging from a case with a buoyant core (denoted *A*), to a neutrally buoyant example (case *B*), then to cases with an increasingly denser core (cases *C*, *D* and *E*). For each test, table 1 summarises the core composition and fluid densities; also provided are estimates of the core fluid viscosity, based on the pressure drop observed when using that fluid alone in the pipe. Note that to achieve higher densities and viscosities for the core fluid, sand and other additives were used for the last two cases. The significance of the implied departure from a central Newtonian fluid is not clear, although the core is not expected to play a decisive role in the dynamics. Post-experiment characterisation of the elastic tube revealed average wall thickness $d \approx 200$ μm measured by callipers, and Young's

modulus $E \approx 0.4$ MPa, determined using ASTM D638 test protocol, the standardised testing method for evaluating tensile properties.

Visualisation of the dynamics of the elastic shell was achieved from one-side of the pipe using a 24.2 megapixel Canon EOS Rebel T7i DSLR camera, with illumination provided by a Dantec Dynamics Ray-Power 5000 continuous-wave laser. Images were captured at a rate of approximately 10 Hz, at an oblique angle of 45° relative to the streamwise axis and subsequently projected onto the transverse plane for quantitative analysis. The imaging system was located at the midpoint of the pipe, well downstream and upstream of any disturbances created by the inflow and outflow. Post-processing involved denoising, binarisation, and segmentation of the image sequence to extract the shell profile. From this, we determined the temporal evolution of the centroid position and cross-sectional area of the visible half of the shell. Given nominal flow speed 0.4 m s^{-1}, the 10 Hz sampling only resolves axial structure over length scales that exceed approximately a pipe diameter.

Figures 2 and 3 show results from the five tests. In the first of these figures, we display renderings from the snapshots of the outline of the shell, first in three dimensions, then superposed on a cross-section through the pipe. These observations reveal both axial and angular variations. The axial undulations span several pipe diameters. The angular variations persist throughout the period of observation, correspond to relatively low angular wavenumbers, and are more prominent on the wider side of the annulus. Spectral analysis via a Fourier transform relative to the centroid of the shell (assuming symmetry about the midline) indicates power in the range of angular modes $3 \leqslant m \leqslant 9$, where m is the angular wavenumber. The angular undulations are suggestive of the presence of compressional buckles. Similarly, the axial variations might be the result of axial buckling. However, both features may also have other origins. The axial variations, for example, could equally well result from transient flow disturbances at the relatively high Reynolds numbers of the experiments.

From the outlines of figure 2, we extract measurements of the mean vertical position $\langle \chi \rangle$ of the shell, and a measure of flatness of the shell $\langle (r_{max} - r_{min})/(r_{max} + r_{min}) \rangle$, as well as data characterising the average gap occupied by the lubricant, $\langle \Xi \rangle$. Averaged over time (which is implied here by the angular brackets), these statistics cluster around well-defined means, as reported in figure 3. It is evident from this figure that when the core is less dense than the surrounding annular fluid, the tube levitates slightly, occupying the upper portion of the pipe cross-section. Conversely, when the core is denser, it settles towards the bottom of the pipe. All the while, a finite gap appears to remain between the core and pipe (for the most part, the measurements of $\langle \Xi_{min} \rangle$ are discernibly bounded away from zero), and the lubricated, encapsulated flow is not hindered by any settling of the core onto the pipe wall. The simple monotonic relation between the mean vertical positions and the density difference supports the conclusion that stable pipelining is feasible.

A comparison of the time-averaged pressure drop per unit length observed for the encapsulated core–annular flows with those for the core fluid alone gives further indication of the capacity for drag reduction. For example, for the cases with heavier core fluids, we observe pressure drops of 22 Pa m^{-1} (case E) and 140 Pa m^{-1} (case D). At equivalent total volumetric flow rate, the pressure drops observed for the core fluid alone are 90 Pa m^{-1} and 803 Pa m^{-1}, respectively. By contrast, when the core is buoyant and comparable in viscosity to the annular fluid (cases A and C), we observe that the pressure drop increases, suggesting drag enhancement. While these findings are peripheral to the central focus of this study, they are included here as a passing observation to highlight possible implications for transport efficiency.

To summarise, the experiments demonstrate that the introduction of an elastic shell between core fluid and lubricant may promote stable pipelining; they highlight both the

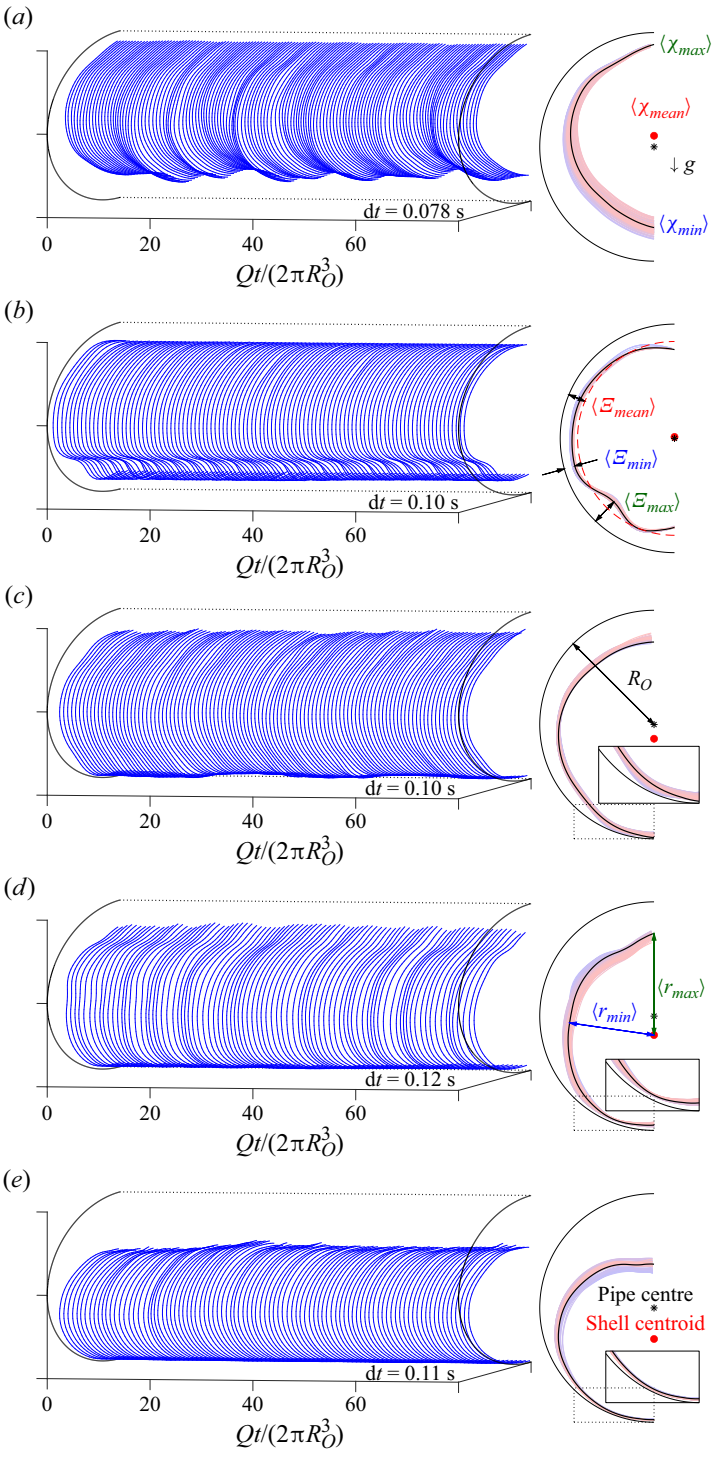

Figure 2. (*a–e*) Snapshots of the elastic shell for the experiments *A–E* listed in table 1, respectively, plotted against time t scaled by the outer radius R_O and the flux Q. In each case, we show snapshots at intervals dt (indicated on the figure), as a three-dimensional rendering on the left, and superposed onto a cross-section through the pipe on the right (colour-coded in time, from blue to red); the time average is shown by the thicker black line. The mean characteristics indicated are plotted as a function of the density difference in figure 3.

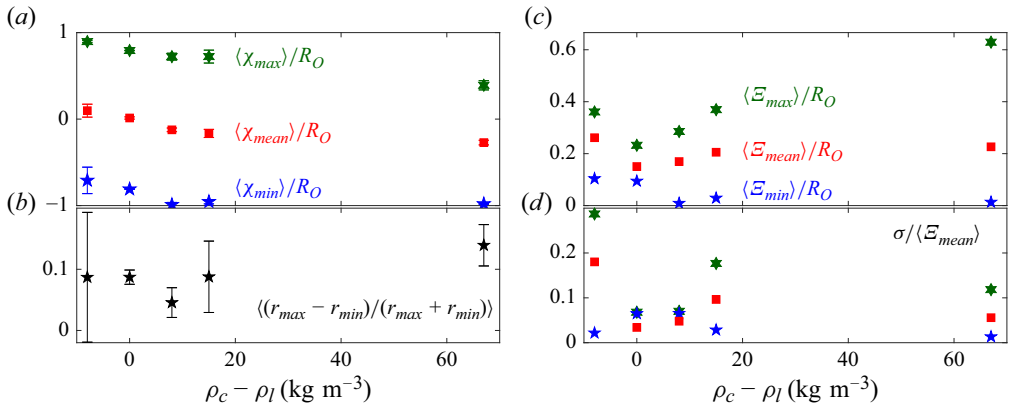

Figure 3. Mean characteristics extracted from the time series in figure 2. (*a*) The mean vertical positions of the shell's centroid, $\langle\chi_{mean}\rangle$, and upper and lower edges, $\langle\chi_{max}\rangle$ and $\langle\chi_{min}\rangle$, scaled by the outer radius R_O. (*b*) The mean flatness of the shell, $\langle(r_{max}-r_{min})/(r_{max}+r_{min})\rangle$, where r is the local radius with respect to the shell centroid. (*c*,*d*) The averages of the maximum, mean and minimum gap thicknesses $\langle\Xi_{max,mean,min}\rangle$ scaled by the outer radius R_O, and their standard deviations $\sigma(\Xi_{max,mean,min})$ scaled by the mean gap. In (*a*,*b*), the error bars show twice the standard deviations of the data.

feasibility of the technology and its potential for practical implementation. The novelty of the configuration in the context of core–annular flows then motivates general modelling studies, such as that outlined below.

3. Model formulation

3.1. *Set-up*

As sketched in figure 1(*b*), we consider an elastic cylindrical shell containing a viscous fluid within a pipe of radius R_O; a less viscous fluid lubricant lies between the shell and the inner surface of the pipe. The geometry is described by cylindrical polar coordinates (r, θ, z), with the angle measured relative to the vertical. Both the shell and the lubricating film are relatively thin, so that the core fluid almost fills the pipe. The shell has undeformed thickness d, which we assume to be of the same order as the characteristic thickness D of the narrow annular gap filled by the lubricant. There is differential motion between shell and pipe: either the shell conveys the core down the pipe with mean speed U_W, or the shell sits largely in place with the pipe translating at speed U_W. We assume that there is no net differential motion between core fluid and shell; when the shell deforms, the pipe geometry limits radial deformations to $O(D)$. Since the core occupies a much larger area than the lubricant, the viscous stresses and pressure perturbations are much smaller, therefore we neglect perturbations there. Consequently, in the frame of the shell, the core fluid is mostly stationary and held at hydrostatic pressure. The core fluid has viscosity μ_c and density ρ_c; the values for the lubricant are μ_l and ρ_l. The shell has Young's modulus E, and undeformed radius R. Gravity g acts in the vertical direction, and we neglect inertia in both the fluid and the solid.

The fluid–structure interaction generated by flow, solid stresses or gravitational loading leads to the deformation of the shell within the pipe. The von Kármán–Donnell model (Yamaki 1984) applies in the bending limit, wherein deformations are mostly in the radial direction and take place at nearly constant thickness d. Radial deflections are $O(d)$ (or $O(D)$), and take place over a much larger characteristic length scale L within the local tangent plane to the shell, where $L^2 = Rd$. Displacements within the tangent plane (i.e. in the

angular and axial directions) are smaller than the radial deflection by order $\epsilon = d/L \ll 1$. Strains in the tangent plane are then $O(\epsilon d/L) = O(d^2/L^2)$, indicating that lateral forces from the associated in-plane net tensions are order Ed^3/L^3. By contrast, the normal force from the bending stress is order Ed^4/L^4. That is, in-plane tension forces exceed radial bending forces by $O(\epsilon^{-1})$.

When flow perturbations in the core remain relatively small, the fluid stresses acting on the surfaces of the shell stem from the two pressures and the viscous stresses in the lubricant. We take the pressures to be comparable, with a characteristic scale $\mathcal{P}$. The viscous stresses are $O(\mu_l U_W/D)$ within the lubricant. The usual balances of lubrication theory imply that $\mu_l U_W/D^2 = O(\mathcal{P}/R)$. Hence the viscous shear stress in the lubricant is $O(\mu_l U_W/D) = O(D\mathcal{P}/R) = O(\epsilon^2\mathcal{P})$; viscous normal stresses are smaller still. The radial load on the shell is therefore dominated by the two fluid pressures, leading us to take the dimensionless group

$$\frac{L^4\mathcal{P}}{Ed^4} \equiv \frac{R^2\mathcal{P}}{Ed^2} \tag{3.1}$$

to be order unity. By contrast, the tension forces in the local tangent plane generated by radial or lateral deflections (of $O(Ed^3/L^3) \equiv O(L\mathcal{P}/d) = O(\epsilon^{-1}\mathcal{P})$) far outweigh the traction on the shell exerted by the lubricant due to the viscous shear stress (of $O(\mu_l U_W/D) = O(\epsilon^2\mathcal{P})$). The shell is therefore impacted primarily by the radial pressure loading, not the axial or angular viscous tractions (cf. Lighthill 1969; Skotheim & Mahadevan 2004; Kodio, Griffiths & Vella 2017; Warburton, Hewitt & Neufeld 2020).

3.2. *Cylindrical shell model*

We denote the local displacements of the midsection of the shell by (X, Y, Z), in the coordinate directions (r, θ, z). In the von Kármán–Donnell shell model (Yamaki 1984), the local strains are given by

$$\varepsilon_1 = \frac{\partial Z}{\partial z} + \frac{1}{2}\left(\frac{\partial X}{\partial z}\right)^2, \quad \varepsilon_2 = \frac{\partial Y}{\partial y} + \frac{X}{R} + \frac{1}{2}\left(\frac{\partial X}{\partial y}\right)^2, \quad \gamma = \frac{\partial Z}{\partial y} + \frac{\partial Y}{\partial z} + \frac{\partial X}{\partial y}\frac{\partial X}{\partial z}, \tag{3.2}$$

and are related to the net tensions by

$$N_z = \frac{dE}{1-\nu^2}(\varepsilon_1 + \nu\varepsilon_2), \quad N_y = \frac{dE}{1-\nu^2}(\varepsilon_2 + \nu\varepsilon_1), \quad N_{yz} = \frac{dE\gamma}{2(1+\nu)}, \tag{3.3}$$

where ν is the Poisson ratio. Here, derivatives with respect to the local Cartesian coordinate y are related to angular ones by $\partial/\partial y \equiv R^{-1}\,\partial/\partial\theta$. Since $X = O(d)$ and $(Y, Z) = O(\epsilon d)$, but $(\partial/\partial y, \partial/\partial z) = O(L^{-1})$ and $R^{-1} = O(\epsilon L^{-1})$, all terms in the strain components are of comparable size.

The equations of net force balance are

$$\frac{\partial N_z}{\partial z} + \frac{\partial N_{yz}}{\partial y} = 0, \quad \frac{\partial N_y}{\partial y} + \frac{\partial N_{yz}}{\partial z} = 0, \tag{3.4}$$

$$\frac{Ed^3\,\nabla^4 X}{12(1-\nu^2)} - N_y\frac{\partial^2 X}{\partial y^2} - 2N_{yz}\frac{\partial^2 X}{\partial y\,\partial z} - N_z\frac{\partial^2 X}{\partial z^2} + \frac{N_y}{R} = q, \tag{3.5}$$

where q denotes the radial pressure loading, and we have neglected the axial and angular loading, in line with earlier comments. We have further omitted any gravitational forces on the shell because of its thinness: such forces are of order $\rho_s g d$, whereas hydrostatic

pressure differences between the core and lubricant are $O((\rho_c - \rho_l)gR)$. We take the latter to be comparable to $\mathcal{P}$ (and the radial load); the neglected gravity forces are smaller by a factor of $O(d/R) = O(\epsilon^2)$ whenever density differences are $O(1)$.

3.3. *Fluid flow*

Because the shell deforms radially only to $O(d)$ (or $O(D)$), and the lateral deflections are even smaller, fluid motions within the core remain small. Consequently, the core fluid is held largely at hydrostatic pressure with

$$p \sim P_c - \rho_c g r \cos\theta, \tag{3.6}$$

where P_c is a constant core pressure.

For the lubricant flow, we appeal to lubrication theory: because radial derivatives are relatively large, the main terms in the force balance equations are

$$\begin{aligned} \frac{\partial p}{\partial r} &\sim 0, \\ \frac{\partial p}{\partial \theta} &\sim \mu_l R \frac{\partial^2 v}{\partial r^2} + \rho_l g R \sin\theta, \\ \frac{\partial p}{\partial z} &\sim \mu_l \frac{\partial^2 w}{\partial r^2}. \end{aligned} \tag{3.7}$$

The pressure is therefore almost uniform across the narrow gap, leading us to set

$$p \sim P_l + \Pi(\theta, z, t) - \rho_l g R \cos\theta, \tag{3.8}$$

where P_l denotes a constant, mean lubricant pressure, and Π denotes any varying component due to lubrication flow.

We also have the velocity boundary conditions

$$v(R_I, \theta, z, t) \sim v(R_O, \theta, z, t) \sim w(R_I, \theta, z, t) \sim 0, \quad w(R_O, \theta, t) = -U_w, \tag{3.9}$$

where $r = R_I$ denotes the inner radius of the gap. The flow along the gap is therefore given by

$$\begin{aligned} v &\sim -\frac{1}{2\mu_l R}(r - R_I)(R_O - r)\frac{\partial \Pi}{\partial \theta}, \\ w &\sim -\left(\frac{r - R_I}{R_O - R_I}\right) U_W - \frac{1}{2\mu_l}(r - R_I)(R_O - r)\frac{\partial \Pi}{\partial z}. \end{aligned} \tag{3.10}$$

Mass conservation applied across the thickness of the gap now provides the Reynolds lubrication equation

$$\frac{\partial \Xi}{\partial t} - \frac{1}{2}U_W \frac{\partial \Xi}{\partial z} = \frac{\partial}{\partial \theta}\left(\frac{\Xi^3}{12\mu_l R^2}\frac{\partial \Pi}{\partial \theta}\right) + \frac{\partial}{\partial z}\left[\frac{\Xi^3}{12\mu_l}\frac{\partial \Pi}{\partial z}\right], \tag{3.11}$$

where $\Xi = R_O - R_I$ is the local thickness of the gap.

3.4. *Removing dimensions*

In the von Kármán–Donnell shell theory, the angular and axial scale L is necessarily smaller than the shell radius R. As a consequence, the Cartesian coordinate y of the local tangent plane becomes divorced from the angular arc length $R\theta$. But the angle θ still appears in the model equations independently of y through the gravitational terms and periodic boundary conditions. Thus, in principle, the model contains multiple angular

coordinates in the style of a multiple scales theory. We abandon this awkward feature of the model by reconstituting both angular variables into the single coordinate θ. Formally, the approximations inherent in the shell are then strictly only small when bending has angular (and axial) scales that are relatively small.

Given this simplification, we remove dimensions by introducing the scalings

$$(r, y, z) = R(\hat{r}, \hat{y}, \hat{z}), \quad (X, Y, Z) = D(\hat{X}, \hat{Y}, \hat{Z}), \quad N_{y,z,yz} = \frac{dDE}{R}\hat{N}_{y,z,yz}, \tag{3.12}$$

$$(q, \Pi, P_c, P_l) = \mathcal{P}(\hat{q}, \hat{\Pi}, \hat{P}_c, \hat{P}_l), \quad (v, w) = U_W(\hat{v}, \hat{w}), \quad \Xi = D\hat{\Xi}, \quad t = \frac{12\mu_l R^2 \hat{t}}{\mathcal{P}D^2}. \tag{3.13}$$

Then, after dropping the hats, the shell equations become

$$N_z = \frac{Z_z + \frac{1}{2}\delta X_z^2 + \nu\left(Y_y + X + \frac{1}{2}\delta X_y^2\right)}{1-\nu^2}, \tag{3.14}$$

$$N_y = \frac{Y_y + X + \frac{1}{2}\delta X_y^2 + \nu\left(Z_z + \frac{1}{2}\delta X_z^2\right)}{1-\nu^2}, \tag{3.15}$$

$$N_{yz} = \frac{Z_y + Y_z + \delta X_y X_z}{2(1+\nu)} \tag{3.16}$$

and

$$\mathcal{B}\nabla^4 X + N_y - \delta(N_z X_{zz} + 2N_{yz}X_{yz} + N_y X_{yy}) = q, \tag{3.17}$$

where

$$\delta = \frac{D}{R}, \quad \mathcal{B} = \frac{d^2}{12R^2(1-\nu^2)}, \tag{3.18}$$

and we select the pressure scale so that

$$\mathcal{P} = \frac{dDE}{R^2}. \tag{3.19}$$

But for the switch in notation, (3.4) remain unchanged. Note that formally, the aspect ratio δ and dimensionless bending stiffness $\mathcal{B}$ are small, but the shortness of bending lengths returns all terms in (3.14)–(3.17) to comparable order. Also, we have employed a shorthand notation, using subscripts z, θ and t to denote partial derivatives, except in the case of the net tensions, $\{N_y, N_z, N_{yz}\}$.

For the core, we obtain

$$p = P_c - \frac{\rho_c g R}{\mathcal{P}} r\cos\theta, \tag{3.20}$$

assuming that $\rho_c g = O(\mathcal{P}/R)$.

The outer lubrication equation becomes

$$\Xi_t - \mathcal{U}\Xi_z = (\Xi^3\Pi_\theta)_\theta + [\Xi^3\Pi_z]_z, \tag{3.21}$$

where

$$\mathcal{U} = \frac{6\mu_l R U_W}{D^2\mathcal{P}}. \tag{3.22}$$

To complete the model, we must connect the radial deformation and loading of the shell with the geometry of the lubrication gap and the pressure difference between the two fluids, as well as providing suitable boundary conditions. The local thickness of the gap Ξ is necessarily connected to the shell's radial deflection X because the shell deforms at constant thickness. However, the shell deflection is also defined with respect to the centreline of the shell, and any net offset should not contribute to the implied bending and tension forces. Therefore,

$$\Xi = 1 + \Delta\cos(\theta - \theta_*) - (X - X_0), \tag{3.23}$$

where X_0 denotes any mean radial displacement, and $\Delta(t)$ denotes the offset of the centreline of the shell (scaled by thickness d) in the angular direction $\theta = \theta_*(t)$.

The pressure jump across the shell is given by

$$q = -P - \Pi - \mathcal{G}\cos\theta, \tag{3.24}$$

where

$$P = P_l - P_c, \quad \mathcal{G} = (\rho_c - \rho_l)\frac{gR}{\mathcal{P}}, \tag{3.25}$$

both of which are assumed to be $O(1)$. Finally, the solutions are 2π-periodic in angle θ. We further adopt periodic boundary conditions in z, taking the axial domain length to be ℓ (so that the dimensional pipe length is ℓR).

3.5. *Summary of governing equations*

We now summarise the model equations after recasting them into a slightly different form. First, if we denote a spatial average over the pipe by

$$\langle \ldots \rangle = \int_0^{\ell}\int_0^{2\pi} (\ldots)\,\frac{\mathrm{d}\theta}{2\pi}\,\frac{\mathrm{d}z}{\ell} \tag{3.26}$$

(rather than the time-average implied in § 2), then the mean tensions are specified to be

$$\langle N_y \rangle = \frac{\left\langle X + \frac{1}{2}\delta(X_\theta^2 + \nu X_z^2)\right\rangle}{1-\nu^2}, \tag{3.27}$$

$$\langle N_z \rangle = \frac{\left\langle \nu X + \frac{1}{2}\delta(\nu X_\theta^2 + X_z^2)\right\rangle}{1-\nu^2}, \tag{3.28}$$

$$\langle N_{yz} \rangle = \frac{\langle \delta X_\theta X_z\rangle}{2(1+\nu)}. \tag{3.29}$$

We then introduce a stress function $F(\theta, z, t)$ (Yamaki 1984) by

$$N_y = \langle N_y\rangle + F_{zz}, \quad N_z = \langle N_z\rangle + F_{\theta\theta}, \quad N_{yz} = \langle N_{yz}\rangle - F_{\theta z}, \tag{3.30}$$

which automatically takes care of the force balance equations in (3.4). Defined in this way, the stress function has no spatial average, and satisfies a biharmonic equation after the elimination of Y and Z using (3.30) and (3.14)–(3.16) (which is stated below).

Our model now reduces to three equations for the thickness and lubrication pressure of the outer layer, Ξ and Π, and the stress function F:

$$\Xi_t + \mathcal{U}\Xi_z - (\Xi^3\Pi_\theta)_\theta - [\Xi^3\Pi_z]_z = 0, \tag{3.31}$$

$$\mathcal{B}\nabla^4 X + N_y - \delta(N_z X_{zz} + 2N_{yz}X_{\theta z} + N_y X_{\theta\theta}) = -P - \mathcal{G}\cos\theta - \Pi, \tag{3.32}$$

$$\nabla^4 F - X_{zz} + \delta(X_{\theta\theta}X_{zz} - X_{\theta z}^2) = 0, \tag{3.33}$$

along with (3.30) and (3.23).

Note that an integral of (3.31) over the entire pipe implies that

$$\frac{\mathrm{d}}{\mathrm{d}t}\langle \Xi \rangle = 0, \tag{3.34}$$

or $\langle \Xi \rangle = 1$ (and $\langle X \rangle = X_0$). Moreover, the net eccentricity of that layer is entirely due to the shift of the centreline of the shell:

$$\left\langle \begin{array}{c} \Xi \cos\theta \\ \Xi \sin\theta \end{array} \right\rangle = \frac{1}{2}\Delta \begin{pmatrix} \cos\theta_* \\ \sin\theta_* \end{pmatrix}, \quad \text{or} \quad \langle X\cos\theta \rangle = \langle X \sin\theta \rangle = 0. \tag{3.35}$$

In fact, the radial force balance in (3.32) can be resolved into the vertical and horizontal directions, then averaged, to arrive at the net force balance conditions

$$\begin{aligned} &\left\langle \left(\mathcal{B}\nabla^4 X + N_y - \delta\left(N_z X_{zz} + 2N_{yz}X_{\theta z} + N_y X_{\theta\theta}\right)\right) \begin{pmatrix} \cos\theta \\ -\sin\theta \end{pmatrix} \right\rangle \\ &= \left\langle (-P - \mathcal{G}\cos\theta - \Pi) \begin{pmatrix} \cos\theta \\ -\sin\theta \end{pmatrix} \right\rangle. \end{aligned} \tag{3.36}$$

After a little algebra, and introducing (3.35), we find

$$\left\langle N_y X \begin{pmatrix} \cos\theta \\ -\sin\theta \end{pmatrix} \right\rangle = -\left\langle \Pi \begin{pmatrix} \cos\theta \\ -\sin\theta \end{pmatrix} \right\rangle - \begin{pmatrix} \frac{1}{2}\mathcal{G} \\ 0 \end{pmatrix}. \tag{3.37}$$

If the angular tension is constant in space, then the left-hand side vanishes in view of (3.35). Equation (3.37) then demands that the net vertical and horizontal forces on the shell due to the lubricating fluid must vanish. In principle, one should similarly consider the axial net force balance, which ultimately dictates U_W when that speed is not set independently. We ignore this detail, however, assuming simply that U_W has been appropriately chosen and does not change in view of the dynamics.

We next employ the model system in (3.31)–(3.33) to explore the deformation of the shell under radial compression, and its vertical translation under the force of buoyancy. As part of this exercise, we solve the equations numerically. We perform these computations by first discretising spatial coordinates on a two-dimensional grid. We then use a Fourier spectral method to deal with the spatial derivatives (Trefethen 2000), solving the resulting coupled ordinary differential equations in time with a standard stiff time integrator (the in-built function ode15s in MATLAB). Henceforth, for brevity, we set the thickness of the shell equal to the initial thickness of the lubricating layer ($d = D$), so that

$$\mathcal{B} = \frac{\delta^2}{12(1-\nu^2)}. \tag{3.38}$$

4. Linear buckling instability

When $\mathcal{G} = 0$, the model equations admit circular base states under uniform radial compression with $\Xi = 1$, $X = X_0$ and $\Delta = Y = \Pi = N_{yz} = 0$. In the absence of axial tension, $N_z = 0$, the base state must have azimuthal tension

$$N_y = N_{y_0} = -P = X_0, \tag{4.1}$$

and the Poisson effect implies an axial strain $Z_z = -\nu N_{y_0}$. Alternatively, if there is no mean axial strain, $Z = 0$, then the base state must have tensions

$$(N_y, N_z) = (N_{y_0}, N_{z_0}) = -P(1, \nu) = -\frac{(1,\nu)X_0}{1-\nu^2}. \tag{4.2}$$

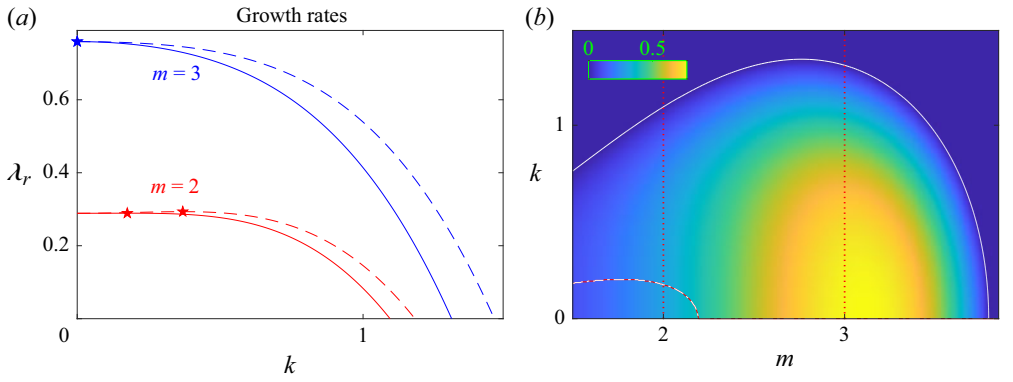

Figure 4. (*a*) Growth rate against k with fixed $m = 2$ and 3, for zero axial stress (solid) and zero axial strain (dashed), for $(P, \nu, \delta, \mathcal{G}) = (1/5, 1/2, 1/8, 0)$. Stars indicate the most unstable wavenumber k in each case. (*b*) Growth rate as a density on the (m, k)-plane for the case with zero axial stress. The stability boundary is shown by the white, solid curve, whereas the (red and white) dash-dotted curve shows the locus of maximum growth (occurring at $k > 0$). The red dotted lines highlight the growth rates for $m = 2$ and 3 plotted in (*a*).

To explore the linear stability of this base state, we set

$$(\Xi, X, \Pi, F) = (1, X_0, 0, 0) + (\tilde{\Xi}, \tilde{X}, \tilde{\Pi}, \tilde{F})\, \mathrm{e}^{\lambda t + \mathrm{i}m\theta + \mathrm{i}kz}, \tag{4.3}$$

with growth rate λ and wavenumbers (m, k). The amplitudes (identified by the tildes), satisfy

$$(\lambda + \mathrm{i}k\mathcal{U})\, \tilde{\Xi} = -(m^2 + k^2)\tilde{\Pi}, \tag{4.4}$$

$$\left[\mathcal{B}(m^2 + k^2)^2 + \delta(k^2 N_{z_0} + m^2 N_{y_0})\right]\tilde{X} - k^2 \tilde{F} = -\tilde{\Pi}, \tag{4.5}$$

$$(m^2 + k^2)^2 \tilde{F} = -k^2 \tilde{X} \quad \text{and} \quad \tilde{\Xi} = -\tilde{X}. \tag{4.6}$$

Thus

$$\lambda = -\mathrm{i}k\mathcal{U} - (m^2 + k^2)\left[\delta(m^2 N_{y_0} + k^2 N_{z_0}) + \mathcal{B}(m^2 + k^2)^2 + \frac{k^4}{(m^2 + k^2)^2}\right]. \tag{4.7}$$

This linear stability analysis describes the elastic buckling of the shell due to imposed compression, with a time scale set by the surrounding lubrication flow; there are similarities with the plane-layer problems considered by Huang & Suo (2002) and Kodio *et al.* (2017).

Sample growth rates are shown in figure 4 for the case without axial tension in (4.1). Modes with lower values of angular and axial wavenumbers are unstable, with the windows of unstable wavenumbers widening with increasing P. The fastest growing modes invariably have $k = 0$, although at fixed m, the most unstable mode possesses finite axial wavenumber once P is sufficiently large. For the parameter settings in figure 4, the growth rate of the $m = 2$ mode is the only one to develop a maximum at finite k, and modes with $m > 3$ remain stable. The results are similar for a base state with zero mean axial strain (4.1), although modes are unstable for somewhat higher axial wavenumbers; see figure 4(*a*).

5. Angular actuation

Progressing beyond linear theory, we first consider purely angular problems in which the shell has no axial variation (dependence on z). For this situation, we rewrite the model

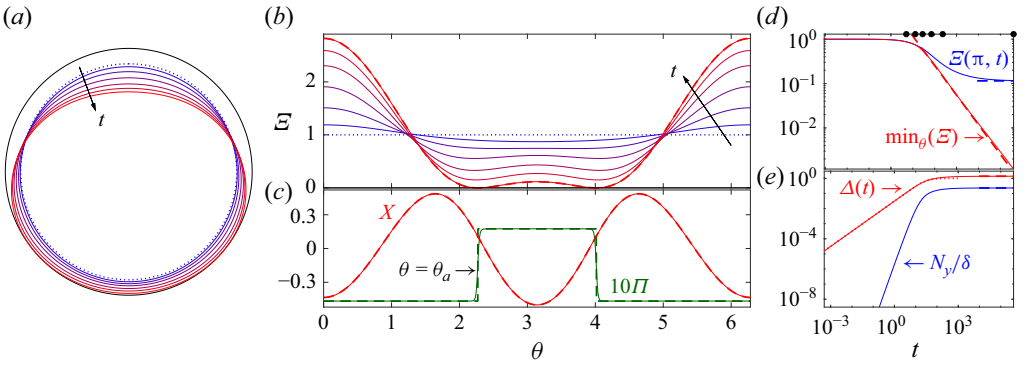

Figure 5. Numerical solution to the pure sedimentation problem, $(P, \nu, \delta, \mathcal{G}) = (0, 1/2, 1/8, 1/32)$. (*a*) Snapshots of the shell (with time increasing from blue to red, as shown by the arrow) in the cross-section. The dotted circle is the initial condition. (*b*) Snapshots of Ξ at the same times. (*c*) The final pressure profile (green) and shell displacement X (red). The dashed lines show the final profiles predicted by the analysis in § 5.1. (*d,e*) Time series of $[\Xi(\pi, t), \min_\theta(\Xi)]$ and $[N_y(t), \Delta(t)]$, respectively. The dashed lines again show the predicted final values in (5.8). The circles in (*d*) indicate the times of the snapshots in (*a,b*), and the red dotted line in (*e*) shows the early-time prediction in (5.6).

equations (3.31)–(3.32) in the form

$$\Xi_t = (\Pi_\theta \Xi^3)_\theta, \quad \Xi = \Xi_0 + \Delta(t)\cos\theta - (X - X_0), \tag{5.1}$$

$$\Pi = N_y(\delta X_{\theta\theta} - 1) - P - \mathcal{G}\cos\theta - \mathcal{B}X_{\theta\theta\theta\theta}. \tag{5.2}$$

Instead of (3.33), we have simply that the angular tension N_y depends only on time. Hence

$$N_y(t) = Y_\theta + X + \frac{1}{2}\delta X_\theta^2 = \left\langle X + \frac{1}{2}\delta X_\theta^2 \right\rangle, \tag{5.3}$$

after an integral over angle. Multiplying (5.2) by $\cos\theta$ and integrating over angle provides an expression equivalent to net vertical force balance:

$$\langle \mathcal{G}\cos\theta + \Pi\cos\theta \rangle = \frac{1}{2}\mathcal{G} - \langle \Pi_\theta \sin\theta \rangle = 0 \tag{5.4}$$

(given $\langle X\cos\theta \rangle = 0$).

5.1. *Pure sedimentation*

For pure sedimentation, we set $P = X_0 = 0$ and consider the fate of the shell as it descends under gravity from an initially centred, circular shape: $\Xi(\theta, 0) = 1$ and $X(\theta, 0) = 0$. A numerical solution to this sedimentation problem is shown in figure 5. Initially, the shell sinks under the weight of the core fluid and remains largely circular because lubrication pressures arising from the underlying squeeze flow are not sufficient to induce significant elastic deformation. Consequently, $|X| \ll 1$ and, from (5.1), we have

$$\dot\Delta\cos\theta = (\Pi_\theta \Xi^3)_\theta, \quad \text{or} \quad \Pi_\theta = \frac{\dot\Delta\sin\theta}{(\Xi_0 + \Delta\cos\theta)^3}. \tag{5.5}$$

Hence, using (5.4),

$$\frac{1}{2}\mathcal{G} = \frac{\dot\Delta}{2(\Xi_0 - \Delta^2)^{3/2}}, \quad \text{or} \quad \Delta = \frac{\Xi_0^3 \mathcal{G} t}{\sqrt{1 + (\Xi_0^2 \mathcal{G} t)^2}}. \tag{5.6}$$

The initial fall is therefore given by $\Delta \sim \Xi_0^3 \mathcal{G} t$. Moreover, if the shell never deforms, then the gap is predicted to close like $\Xi_0 - \Delta \sim (1/2)\Xi_0^{-3}(\mathcal{G}t)^{-2}$, as in other viscous contact problems (Brenner 1961; Cawthorn & Balmforth 2010).

Eventually, however, the shell descends to positions at which the lower surface closes towards contact with the outer wall, raising the local squeeze-flow pressure. The shell then deforms into a roughly elliptical shape (figure 5*a*). In more detail, the high pressures reached underneath the lowest part of the shell prevent closure there. Instead, a small pocket of the lubricant becomes permanently trapped against the bottom of the pipe (figure 5*b*). The minimum gap is then no longer located at $\theta = \pi$ but becomes shifted to two symmetrical locations on either side, $\theta = \theta_a$ and $\theta = 2\pi - \theta_a$. That gap continues to thin inexorably (figure 5*c*), and the dynamics is similar to that for the sedimentation of a rigid cylinder against a bending beam (Balmforth, Cawthorn & Craster 2010).

Note that $N_\theta \equiv (1/2)\delta\langle X_\theta^2\rangle$ when $\langle X\rangle = 0$. Therefore, even though one might imagine that radial displacements with $X < 0$ and $|X| > (1/2)\delta X_\theta^2$ might be sufficient to induce local compression, the angular strain Y_θ is always sufficient to ensure that $N_y > 0$, and the shell remains under tension during pure sedimentation (figure 5*d*).

The rate at which the off-centre minimum gaps close can be extracted using an analysis similar to that given by Balmforth *et al.* (2010): the relatively high pressure maintained in the pocket balances both the weight of the core fluid and the low pressure arising in the remainder of the gap. At asymptotically large times, both these pressures become nearly uniform in θ, with sharp pressure jumps arising over the minimum gaps. The shape of the shell is then set by solving $\Pi \sim \Pi_a$ over the pocket, and $\Pi \sim \Pi_b$ over the rest of the gap. The constrictions at $\theta = \theta_a$ and $\theta = 2\pi - \theta_a$ are too narrow to permit sharp changes in the lower angular derivatives of $X(\theta)$. Hence $\Xi = \Xi' = 0$, whereas X'' and X''' are continuous at those points. The limiting shape of the shell is then given by solving the two versions of (5.2) with $\Pi \sim \Pi_a$ or $\Pi \sim \Pi_b$, subject to these conditions, plus (5.3) and the constraints $\langle X\rangle = \langle X\cos\theta\rangle = 0$ and $X'(0) = X'''(0) = X'(\pi) = X'''(\pi) = 0$. Figure 5(*b*) includes the resulting predictions for $\Xi(\theta)$ and Π.

The constrictions at $\theta = \theta_a$ and $\theta = 2\pi - \theta_a$ provide bottlenecks through which the fluid in the pocket leaks out. For the first of these, the gap is locally given by $\Xi \sim (1/2)\Xi''(\theta_a)(\theta - \theta_a)^2 + \Upsilon$, where the minimum thickness in angle is $\Upsilon(t) = O(\theta - \theta_a)^2 \ll 1$ (which follows because of (5.2) and the conditions that match the bottlenecks of the pocket to the main gap; see Balmforth *et al.* 2010). But the flux through the constriction must equal half the rate of decrease of the pocket's area. Hence

$$-\Xi^3\Pi_\theta \sim (\pi - \theta_a)\dot{\Upsilon}, \quad \text{or} \quad \Pi_\theta \sim -\frac{(\pi - \theta_a)\dot{\Upsilon}}{\left[\frac{1}{2}\Xi''(\theta_a)(\theta - \theta_a)^2 + \Upsilon\right]^3}. \tag{5.7}$$

Integrating this relation across the constriction gives

$$\Pi_a - \Pi_b \sim \frac{3\pi}{8}(\pi - \theta_a)\Upsilon^{-5/2}\dot{\Upsilon}\sqrt{\frac{2}{\Xi''(\theta_a)}}, \quad \text{or} \quad \Upsilon \sim \left[\frac{\pi^2(\pi - \theta_a)^2}{8(\Pi_a - \Pi_b)^2\Xi''(\theta_a)}\right]^{1/3} t^{-2/3}. \tag{5.8}$$

The predictions above match well with late-time numerical solutions provided that $\mathcal{G}$ remains less than some critical value: with strengthening gravity, the pressurised pocket trapped by the constrictions becomes less effective in supporting the weight of the core fluid. As a result, the roof of the pocket begins to bend downwards once $\mathcal{G}$ is raised sufficiently, until $\Xi \to 0$ at $\theta = \pi$ for $\mathcal{G} \approx 0.155$, with the other parameter settings chosen for figure 5. Beyond this threshold, the steady solutions constructed above cease to exist.

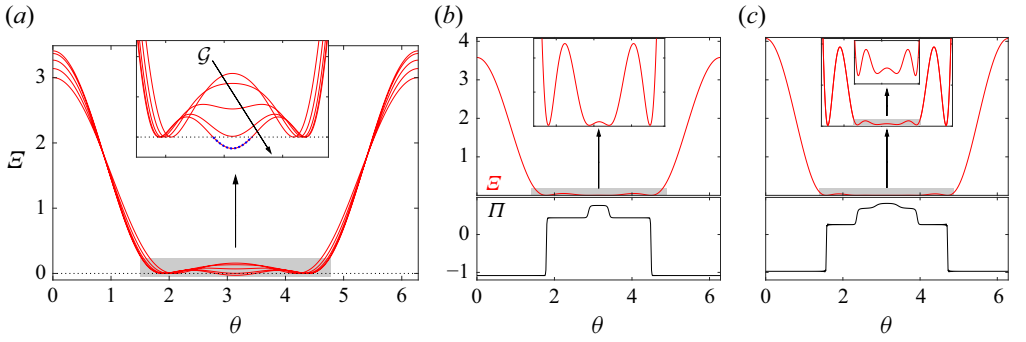

Figure 6. Steady solutions for pure sedimentation with varying $\mathcal{G}$, allowing contact at $\theta = \theta_a$ and $2\pi - \theta_a$, for $(P, \nu, \delta) = (0, 1/2, 1/8)$. (*a*) The local gap $\Xi(\theta)$ for $\mathcal{G} = 1/16, 3/32, 1/8, 0.15, 0.16$ (with $\mathcal{G}$ increasing as shown by the arrow); the inset shows a magnification of the shaded region. The section of the solution for the highest value of $\mathcal{G}$ with $\Xi < 0$ (shown by the blue dotted line) is unphysical. On the right are late-time numerical solutions of the initial-value problem for sedimentation with (*b*) $\mathcal{G} = 1/4$ and (*c*) $\mathcal{G} = 3/4$. Both Ξ and the pressure Π are plotted at $t = 4 \times 10^5$.

Figure 6(*a*) shows a sequence of the steady solution for values of $\mathcal{G}$ increasing up to, and then beyond, the threshold. Once the steady solution predicts negative gaps around $\theta = \pi$, the solutions to the initial-value problem follow a slightly different evolution: at two new points of constrictions straddling $\theta = \pi$, the shell bends down towards contact with the outer pipe. Those constrictions now trap a new pocket inside the original one, possessing a yet higher pressure. The original pocket at that stage splits into two satellites to either side. Figure 6(*b*) show a late-time solution illustrating the creation of nested pockets for $\mathcal{G} = 1/4$. The final steady states could, in principle, be built by generalising the analysis above and adding more contact points.

For even higher gravity, the nested pockets again fail to support the core fluid, and the roof of the central pocket again bends down to the outer pipe. The sequence then repeats, more constrictions appearing along with another, higher pressure pocket, now with two satellites on either side. Figure 6(*c*) shows a third, late-time solution for $\mathcal{G} = 3/4$, in which five pockets emerge in this manner. Although we have not verified this, it seems plausible that a continued increase in $\mathcal{G}$ could lead to the generating of an arbitrary number of constrictions and pockets.

Note that the inexorable sedimentation exposed above can be arrested by adding an angular differential rotation between the shell and the pipe, all the while maintaining the simplicity of the purely angular two-dimensional problem. This inclusion requires an extension of our model formulation, and is discussed in more detail in Appendix A. The discussion acts as a prelude to that in § 7, where we grapple with achieving levitation in the full three-dimensional problem in which the pipe translates relative to the shell in the axial direction.

5.2. *Basic buckling*

Turning now to buckling without sedimentation, we set $\mathcal{G} = 0$ with $P > 0$. The circular base states have $N_y = X = -P$ and $\Xi = 1$. Linear perturbations to these states with angular wavenumber m have growth rates,

$$\lambda = m^4(\delta P - \mathcal{B}m^2). \tag{5.9}$$

Sample numerical solutions for three values of P are presented in figure 7. In all three cases, the base state is unstable, and the most unstable linear modes with either $m = 2$

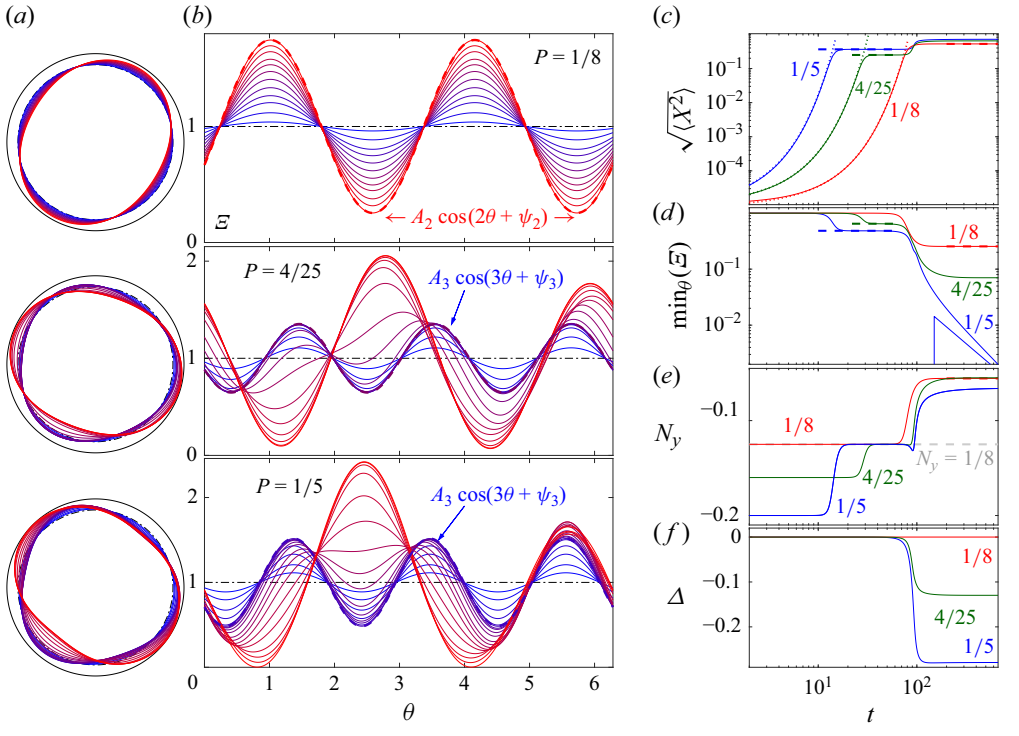

Figure 7. Angular buckling solutions for $P = 1/8$, $4/25$ and $1/5$, for $(\nu, \delta, \mathcal{G}) = (1/2, 1/8, 0)$. Shown are snapshots of (*a*) the cross-section and (*b*) $\Xi(\theta, t)$ (with P increasing from top to bottom). The black dash-dotted lines in (*a*,*b*) plot the initial condition. The thick dashed lines show the prediction in (5.11), as labelled. On the right, we plot the time series of (*c*) $\sqrt{\langle X^2 \rangle}$, (*d*) $\min_\theta(\Xi)$, (*e*) N_y and (*f*) Δ (with $P = 1/8$ in red, $4/25$ in green and $1/5$ in blue). The dashed lines show the predictions in (5.11) (for $m = 2$ at late times, and for $m = 3$ at intermediate times in (*c*–*e*)), with ψ_m chosen to align the zeros of $\Xi - 1$. The dotted lines in (*c*) show the prediction of linear theory, matching amplitudes at $\sqrt{\langle X^2 \rangle} = 0.01$. The triangle in (*d*) indicates the power law $t^{-3/2}$. In each case, the initial condition consists of a superposition of the first twenty angular modes with random phases and amplitudes (of mean 10^{-4}).

or $m = 3$ take over the initial linear growth phase. The modes subsequently saturate into nonlinear, buckled states. For the case with $P = 1/8$, the $m = 2$ buckles persist indefinitely. In the second case, with $P = 4/25$, the $m = 3$ buckles subsequently suffer a secondary instability towards lower wavenumber perturbations. Two of the buckles subsequently merge, leaving an asymmetric $m = 2$ state with buckles of unequal amplitude. In the final case, $P = 1/5$, the initial $m = 3$ mode again suffers a secondary instability towards $m = 2$. This time, however, the buckle amplitudes grow sufficiently to press the two radial maxima into the outer wall. The minimum gap then continues to thin towards contact. This time, however, thinning looks to follow a steeper power law than the $t^{-2/3}$ law seen with sedimentation in (5.8).

The steady, single-mode nonlinear states necessarily have vanishing lubrication pressures $\Pi = 0$, implying that

$$\mathcal{B} X_{\theta\theta\theta\theta} = \delta N_y X_{\theta\theta}. \tag{5.10}$$

Hence

$$X = A_m \cos(m\theta + \psi_m), \quad N_y = -\frac{m^2 \mathcal{B}}{\delta} \quad \text{and} \quad A_m = \frac{2}{m}\sqrt{\frac{P + N_y}{\delta}}, \tag{5.11}$$

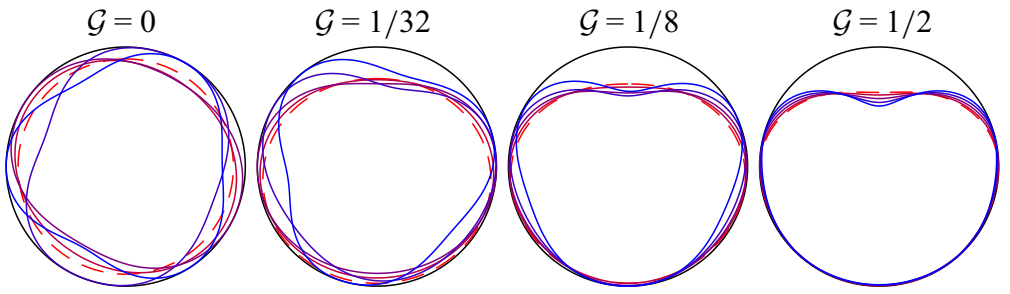

Figure 8. Angular solutions with both buckling and gravity, $(\nu, \delta) = (1/2, 1/8)$. Shown are the final states (at $t = 333$) for solutions with the values of $\mathcal{G}$ indicated. In each image, five cases are plotted with $P = 0, 1/10, 9/40, 9/5, 3/4$ (from dashed red to blue).

where the phase ψ_m is selected during the initial-value problem. If the centreline of the shell is never displaced during buckling, then we also find $\min_\theta(\Xi) = 1 - A_m$. As shown in figure 7(*b*), these predictions align with the numerical solution for $P = 1/8$.

When buckling modes interact nonlinearly, as in the second example of figure 7 with $P = 4/25$, the final state is somewhat similar, but differs in one key respect: the nonlinear mode interaction generates a net displacement of the shell's centreline that cannot be predicted purely from an instantaneous force balance. Indeed, after the initial saturation of the $m = 3$ unstable mode, but before the onset of secondary instability ($t \lesssim 75$), $\Delta \approx 0$ and the tension and deflection are given by (5.11) with $m = 3$; see figure 7(*c–f*). In other words, although the final shell displacement and angular stress are still given by (5.11), the gap thickness Ξ picks up an $m = 1$ component that is prescribed by the dynamics. The final example of figure 7 with $P = 1/5$ is similar, except that the outer wall limits the growth of the final buckle after the secondary instability, so that $\sqrt{\langle X^2 \rangle}$ and N_y never quite reach the expected values from (5.11).

Final buckled states for more values of P are shown on the left of figure 8. Although these examples show solutions for which the most unstable mode increases from $m = 2$ to $m = 5$, the final states possess only two or three nonlinear buckles as a result of coarsening. In the approach to the final state, these buckles rotate somewhat with respect to one another in order to achieve an angular force balance as they press into the wall of the pipe; otherwise, the patterns have arbitrary orientation. Note that the addition of gravity breaks this angular symmetry, as demonstrated by the three other examples on the right of figure 8, which have $\mathcal{G} > 0$: the patterns further reorientate in angle to maintain vertical force balance, an effect that typically improves the degree of left–right symmetry. Sedimentation further forces the shell to conform to the lower parts of the pipe wall, reducing buckling over the narrower sections of the gap. At the highest value of $\mathcal{G}$, the shell adopts the shape of the pipe over more than half of the lower circumference, leaving only a single, inwardly directed buckle at the top.

6. Shell buckles

The linear stability theory of § 4 indicates that the most unstable modes invariably have zero axial wavenumber $k = 0$, suggesting that buckling is purely angular, as considered in § 5.2. However, for fixed, lower angular wavenumber m, modes with finite axial wavenumber can be unstable (see figure 4). An important feature of the angular buckling problem is also that higher-wavenumber buckling patterns can coarsen to create stronger, fewer angular buckles. In combination, one therefore wonders whether the nonlinear

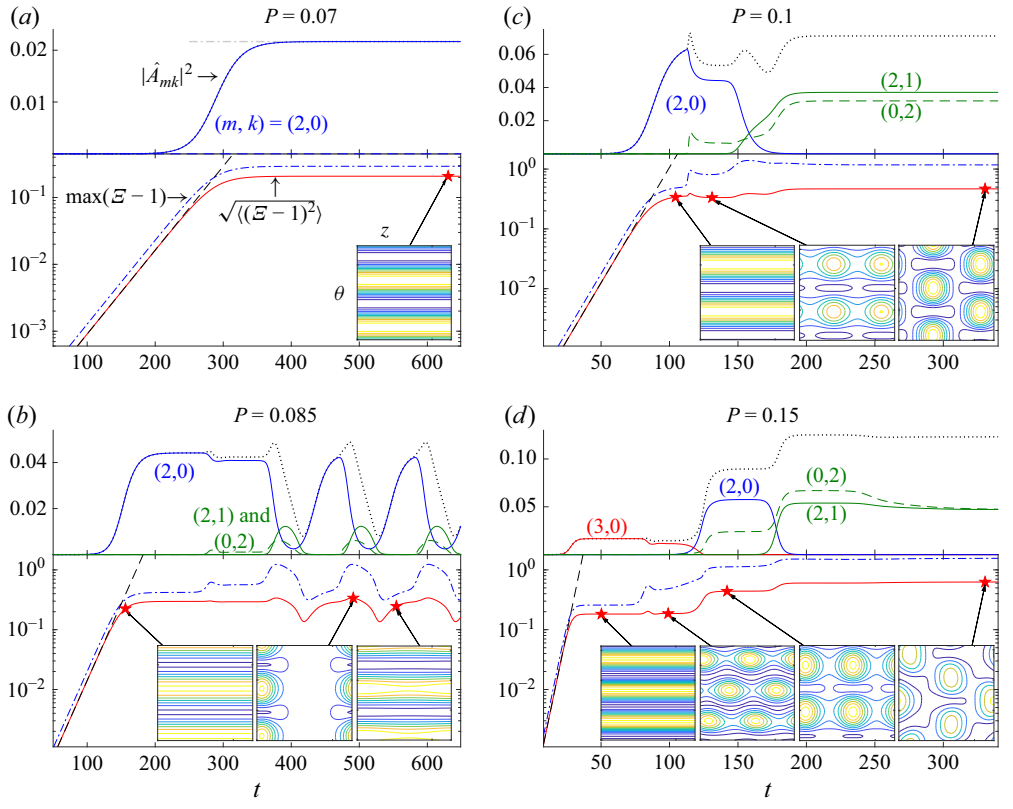

Figure 9. Shell buckling solutions for (*a*) $P = 0.07$, (*b*) 0.085, (*c*) 0.1 and (*d*) 0.15, for $(\nu, \delta, \mathcal{G}) = (1/2, 1/8, 0)$. For each panel, we plot time series of the average $\sqrt{\langle(\Xi - 1)^2\rangle}$ (red solid lines) and maximum (blue dash-dotted lines) gap thickness in the lower half, and the power $|\hat{A}_{mk}|^2$ in the dominant Fourier modes in the upper half. The latter are labelled by their wavenumbers (m, k). The black dotted line indicates the sum of the powers of all Fourier modes. The black dashed lines indicate the exponential growth of the most unstable linear modes (matching amplitudes at $\sqrt{\langle(\Xi - 1)^2\rangle} = 0.01$). The lighter grey dash-dotted line in the upper half of (*a*) shows the expected amplitude of the nonlinear pure mode with $(m, k) = (2, 0)$ as given by (5.11). Insets to each panel show contour maps of the buckle pattern in the (θ, z)-plane at the times indicated by the stars. For each case, the initial condition is given by the most unstable angular mode of linear theory with amplitude of $O(10^{-4})$ and random phase.

buckling dynamics might lead to a preference for states with axial as well as angular buckles, via some sort of secondary instability. To explore this further, we solve the full system (3.31)–(3.33) numerically.

Figure 9 shows sample numerical solutions for four increasing values of P. Plotted are time series of the average and maximum gap thickness, along with the power in the strongest Fourier modes. That is, for the latter and after defining the Fourier series

$$X = X_0 + \sum_{k=0}^{\infty}\sum_{m=0}^{\infty} \hat{A}_{mk}\, \mathrm{e}^{\mathrm{i}(m\theta + kz)} + \text{c.c.}, \tag{6.1}$$

we plot $|\hat{A}_{mk}|^2$ for the modes that achieve the highest amplitudes during some phase of the entire evolution captured by the computations (note that $\hat{A}_{00} = \hat{A}_{10} = 0$ in view of our definition of X_0 and (3.35)). For the cases shown in the figure, these modes have wavenumbers (2, 0) or (3, 0) initially, then a mix of (0, 2) and (2, 1) at later times for all

but the first example. Figure 9 also presents sample buckling patterns on the (z, θ)-plane at certain instants during the evolution where specific patterns emerge.

Linear theory predicts that the $(m, k) = (2, 0)$ mode is most unstable for $0.06 \lesssim P \lesssim 0.125$, but is then replaced by the $(m, k) = (3, 0)$ mode when P is raised above 0.125. The four computations in figure 9 follow the corresponding linear predictions initially (with $(m, k) = (2, 0)$ emerging in figure 9(*a*,*b*,*c*), and (3, 0) appearing in figure 9(*d*)). At later times, the growth of the buckles saturates nonlinearly. For the case with $P = 0.07$ in figure 9(*a*), the resulting buckle becomes steady and is maintained until the end of the computation (at $t = 2 \times 10^3$). Being uniform in the axial direction, this state is described by (5.11). For all the other cases, however, the nonlinear state reached after the initial saturation does not remain stable, but suffers multiple secondary instabilities.

For the examples with $P = 0.085$ and 0.1, the nonlinear state with $(m, k) = (2, 0)$ first becomes interrupted by the growth of a mode with $(m, k) = (0, 2)$ (see the second inset to figure 9*c*). The nonlinear state with both modes does not survive, however, due to the growth of another mode with $(m, k) = (2, 1)$. For $P = 0.085$ and figure 9(*b*), the result is a state that pulsates in time, with what look to be predator–prey-type oscillations between the $(m, k) = (2, 0)$ mode and its interruption by the $(m, k) = (0, 2)$ and (2, 1) modes. With $P = 0.1$ (figure 9*c*), a new nonlinear steady state emerges in which the $(m, k) = (2, 0)$ mode is suppressed. The final pattern then has a chequerboard structure.

For the final example with $P = 0.15$ (figure 9*d*), the saturated $(m, k) = (3, 0)$ mode loses stability to a $(m, k) = (2, 2)$ mode (with the resulting pattern shown in the second inset); neither survives, however, but they are replaced by the $(m, k) = (0, 2)$ and (2, 1) combination (third inset). Finally, $(m, k) = (2, 1)$ again appears, suppressing $(m, k) = (2, 0)$ (fourth inset).

Altogether, the sequence shown in figure 9 illustrates how angular buckling patterns, though most unstable, are not necessarily those realised, except near the onset of instability. The nonlinear dynamics is evidently rich, with a variety of angular and axial buckling patterns possible. The appearance of time-periodic patterns is perhaps most striking, given the relatively viscous lubrication flow that controls the time scale of the dynamics.

7. Elastohydrodynamic lubrication

An important feature of our model is that if the shell is periodic in z, then one can transform into a frame moving with speed $-\mathcal{U}$ to eliminate the advection term in (3.31), i.e. by defining a new axial coordinate $\zeta = z + \mathcal{U}t$. In this new frame, the problem is equivalent to that when the pipe is stationary, in which the core always sediments under gravity. One therefore cannot add the motion of the pipe into the problem to generate a lift force to counter gravity. This implies that the buckled states discussed in the last section cannot generate lift if the wall is translated ($\mathcal{U} > 0$). Instead, some other feature is needed to break the symmetry and counter buoyancy.

Here, we employ a simple device for this task within the framework of the current shell model. In the frame of the core (and shell, in which (3.31) is written), we fix the annular gap at the ends of the domain in z. As this is performed practically at the first and last collocation points (which are $z = 0$ and $2\pi(1 - N^{-1})$ if N denotes the number of axial grid points), the device is equivalent to enforcing clamped boundary conditions at the ends, and means that one can no longer jump into a moving frame to eliminate the advection term.

Figures 10 and 11 display numerical solutions to this problem, setting $(P, \nu, \delta, \mathcal{G}) = (0, 1/2, 1/8, 1)$. The first of these figures displays two snapshots at different times for

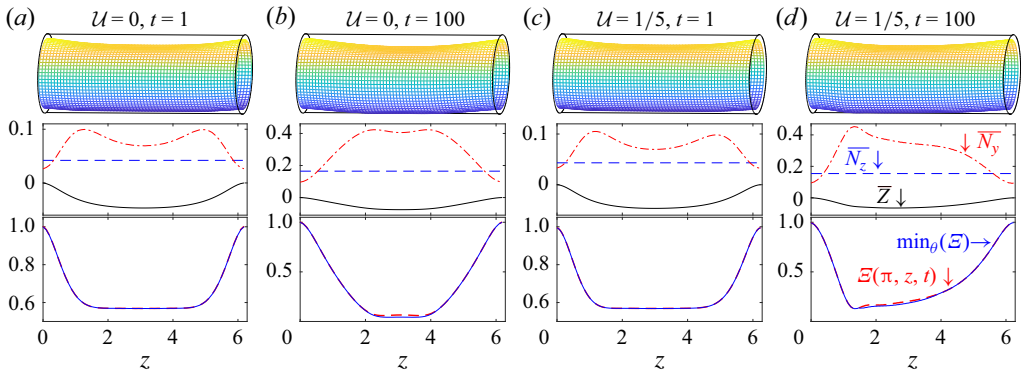

Figure 10. A sedimentation solution with fixed gaps at $x = 0$ and π, for $(P, \nu, \delta, \mathcal{G}) = (0, 1/2, 1/8, 1)$. Shown are a surface plot of the shell (top), the angular averages $\{\overline{N_Y}, \overline{N_Z}, \overline{Z}\}$ (middle) and $\Xi(\pi, z, t)$ and $\min_\theta(\Xi)$ (bottom), for the times and velocities indicated.

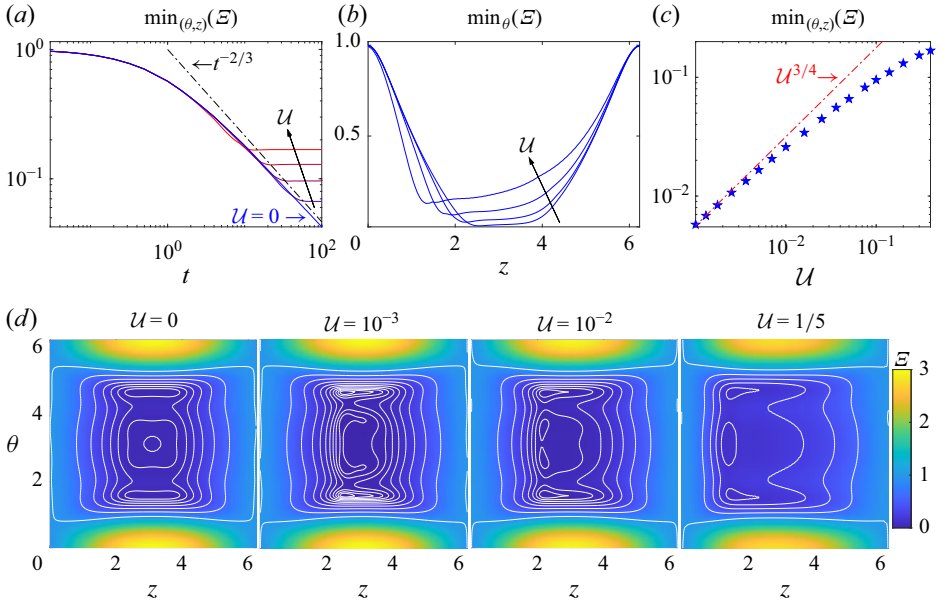

Figure 11. Details of the gap for sedimentation solutions with fixed shell position at $z = 0$ and π and varying $\mathcal{U}$, for $(P, \nu, \delta, \mathcal{G}) = (0, 1/2, 1/8, 1)$. (*a*) Time series of the minimum of the gap over both angle θ and axial position z, for solutions with $\mathcal{U} = 0, 1/20, 1/10, 1/5, 2/5$, (from blue to red). The dash-dotted line shows the power law $t^{-2/3}$. (*b*) The minimum of the gap over angle at the final time ($t = 100$) plotted against axial position z for $\mathcal{U} = 10^{-3}, 10^{-2}, 1/20, 1/5$ (increasing $\mathcal{U}$ shown by the arrow). (*c*) Final minimum gaps over θ and z plotted against $\mathcal{U}$; the dashed line shows the scaling $\mathcal{U}^{3/4}$. (*d*) Density plots on the (z, θ)-plane showing the shape of the final gap thickness $\Xi(\theta, z, 100)$ for $\mathcal{U} = 0, 10^{-3}, 10^{-2}, 1/5$ (from left to right). The white lines show contours at $\Xi = 10^{-j/5}$ for $j = 0, 1, \ldots, 10$.

solutions with two values of $\mathcal{U}$, and shows a three-dimensional rendition of the shell (top row), the angular averages $\{\overline{N_Y}, \overline{N_Z}, \overline{Z}\}$, and details of the gap (the minimum of $\Xi(\theta, z, t)$ over θ and $\Xi(\pi, z, t)$). Here,

$$\overline{f(\theta)} = \int_0^{2\pi} f(\theta)\,\frac{\mathrm{d}\theta}{2\pi}, \tag{7.1}$$

and $\overline{Z} = \overline{\Xi \cos\theta}$ denotes the vertical position of the centroid of the shell. Figure 11 plots further details of the solutions along with some additional cases with different values of $\mathcal{U}$.

In the first example of figure 10 for $\mathcal{U} = 0$, the shell sags in the middle of the domain under the action of gravity on the core fluid; the ends are, however, held in place. The extensions generating by sagging induce mean axial and angular tensions, which contribute to opposing the gravitational fall, but are unable to prevent it. The gap below the lowest section of the shell then continues to thin with time. As shown in the times series of figure 11(*a*), thinning again takes the power-law form $t^{-2/3}$. The narrowing gap itself develops a complicated spatial pattern involving a number of constrictions and trapped pockets, somewhat similar to the purely angular problem of § 5.1; see the first image of figure 11(*d*).

As shown by the second example of figure 10, with $\mathcal{U} = 1/5$, the addition of the motion of the pipe (from right to left in z) changes this dynamics: as fluid is dragged through the gap underneath the shell, the gap becomes asymmetrical about $z = \pi$ (figure 10*c*,*d*) and a lift force is generated. The descent of the shell is then arrested and steady, levitated lubrication is achieved (see figure 11*a*). In other words, the relative motion of the shell and outer wall creates the lift needed to prevent contact, a result aligning with those presented by Ooms and others (e.g. Ooms & Beckers 1972; Ooms & Poesio 2003; Ooms, Vuik & Poesio 2007). As shown in the last image of figure 11(*d*), we again see that the narrow gap underneath the shell becomes deformed into a somewhat complicated spatial pattern.

Solutions with further values of $\mathcal{U}$ are provided in figure 11. In this wider suite of computations, steady levitation is reached over long times whenever there is translation ($\mathcal{U} > 0$). For the final, steady levitated states, the minimum of the gap over angle possesses a profile in z that is similar to the gap profile with θ seen for axially uniform states in steady angular rotation (see Appendix A and figure 12). In both cases, the gap narrows as fluid is dragged underneath the shell, before widening more abruptly on the downstream side of the constriction. The increasing fine structure that develops over the constriction as $\mathcal{U}$ decreases is illustrated by two further density maps of the final gap in figure 11(*d*).

Figure 11(*c*) displays how the minimum gap over both angle θ and axial direction z varies with translation speed $\mathcal{U}$ in the steady states. The minimum appears to follow the scaling $\min_{(\theta,z)}(\Xi) \propto \mathcal{U}^{3/4}$ for $\mathcal{U} \ll 1$, which mirrors the dependence $\Omega^{3/4}$ found for axially uniform, steadily rotating states with dimensionless rotation rate Ω (Appendix A). The latter scaling is analogous to that found for elastohydrodynamic line contacts (e.g. Bissett 1989; Bissett & Spence 1989; Lugt & Morales-Espejel 2011; Snoeijer, Eggers & Venner 2013), and can be understood in a similar fashion by considering the bottlenecks in flow at the ends of the constricted region (see Appendix A). Following Snoeijer *et al.* (2013), who also considered elastohydrodynamic point contacts, we rationalise the scaling $\mathcal{U}^{3/4}$ observed for the axially varying problem by arguing that it must result because flow through the constriction is almost unidirectional, and therefore equivalent to the problem with angular rotation.

8. Conclusion

In this paper, we have presented exploratory laboratory experiments demonstrating stable pipelining of core–annular flow at high Reynolds number. The critical feature of these experiments is the insertion of an elastic shell between the core and lubricating fluid, which deforms to produce distinctive sculpted patterns during transport. The time-averaged position of the shell is levitated when the core fluid is less dense than the surrounding

annular fluid, and descends into a stable, off-centre position when the core is denser. In all configurations examined, a finite gap consistently remains between the core and the pipe wall. These observations lend experimental support to the concept that a three-layer structure in core–annular flows can promote flow stability, an idea originally proposed by Frigaard and collaborators, though they proposed encapsulating the core with a rather different material.

As a complement to these exploratory experiments, we have further presented a reduced model designed to interrogate the dynamics of a cylindrical elastic shell emplaced between the two fluids of a core–annular flow. To construct this reduced model, we introduced a series of simplifying assumptions, taking the lubricating fluid and elastic shell to be thin relative to the pipe radius, and neglecting inertial effects. Although these simplifying assumptions distance the theoretical model from the experiments, several key aspects of the dynamical fluid–structure interaction are captured: buckling under radial compression, sedimentation of the core under density differences, and lift created by elastohydrodynamic effects due to axial translation (or angular rotation).

In the linear stability analysis of buckling under radial compression, we observed that angular wavenumbers are preferred. Our nonlinear computations, however, show that the preferred modes can suffer secondary instabilities in the form of angular buckles that may lead to a coarsening of the angular pattern, or more significantly, the development of axially varying structure. Therefore the model system shows the potential to self-sculpt and form natural axial and angular corrugations. As the shell remains intact, no mixing of the fluids results from this sculpting process, unlike in other core–annular flows.

A sculpted interface is critical for stable transport in horizontal pipelines due to its potential to generate hydrodynamic lift, as noted by Ooms and co-workers. However, the periodic buckled states arising from purely radial compression do not produce lift, as they are symmetric about the horizontal axis. This observation motivated our investigation of configurations in which the ends of the elastic shell are clamped, thereby breaking the left–right symmetry. In this setting, we demonstrate that elastohydrodynamic effects can induce levitation of the core. Further evidence for the role of elastohydrodynamics is provided by our analysis of rotational motion (Appendix A), which also contributes to the generation of lift.

Although some of the physical assumptions in the model are divorced from the original experimental set-up, both theory and experiments build on the proposal that stable pipelining can be achieved by encapsulating the core fluid within an elastic shell. We leave it to future work to extend the model to bring theory closer to experiments. In particular, it remains to incorporate inertia and axial pressure gradients, allow for thicker shells and lubricating layers, and trigger elastohydrodynamic lubrication more realistically than clamping the shell at its ends.

Acknowledgements. We thank the Natural Sciences and Engineering Council of Canada (NSERC) for financial support. T.V.B. gratefully acknowledges support from a Leverhulme Trust Early Career Fellowship (ECF-2022-584).

Declaration of interests. The authors report no conflict of interest.

Appendix A. Levitation by rotation

In this appendix, we discuss the effect of adding a rotational term to (5.1) that models the effect of allowing the outer pipe to rotate relative to the shell. That evolution equation becomes modified to

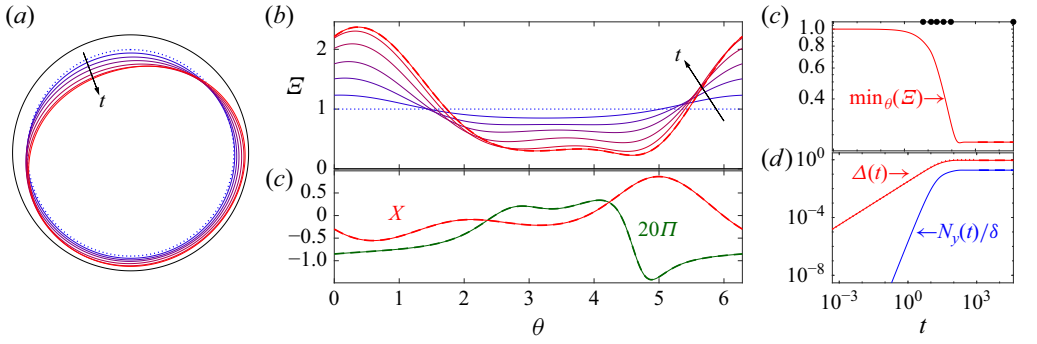

Figure 12. A plot similar to figure 5, but showing sedimentation with rotation for $\Omega = (1/2)\mathcal{G}$, for $(P, \nu, \delta, \mathcal{G}) = (0, 1/2, 1/8, 1/32)$. Only the time series of $\min_\theta(\Xi)$ is plotted in (c), and the dashed lines in (b,c,d) indicate the final steady state.

$$\Xi_t + \Omega\,\Xi_\theta = (\Pi_\theta \Xi^3)_\theta, \tag{A1}$$

where Ω is the dimensionless rotation rate. We include this term to illustrate how the relative motion of the shell and outer cylinder could lead to a lift force that prevents the sedimentation of the shell (cf. Ooms & Beckers 1972), whilst retaining the relatively simple two-dimensional geometry of the angular problem. In doing so, however, we set aside an awkward detail related to how that rotation would impose a torque on the shell to force it to rotate as well.

Figure 12 shows a sample solution with $\Omega = 1/2$, for comparison with figure 5. The initial phase of descent is similar to the case without rotation, but when the shell descends close to the outer rotating wall, viscous shear stresses drag the shell up the side. This breaks the left–right symmetry of the pressure distribution (figure 12*b*), creating a lift force to counter gravity. Consequently, the descent becomes arrested, and no pressurised pocket is trapped between two constrictions against the lowest part of the cylinder. Instead, the gap remains fully open, and the solution converges to a steady levitated state (figure 12*c*).

The steady states can be constructed explicitly by solving

$$Q - \Omega\,\Xi = \Xi^3 \Pi_\theta, \tag{A2}$$

along with (5.2), periodic boundary conditions and the constraints $\langle X\rangle = \langle X\cos\theta\rangle = 0$ and (5.3). Here, Q is the net angular flux, which appears as an eigenvalue. A series of steady states constructed in this way with varying rotation rate is shown in figure 13. As $\Omega \to 0$, the gap closes over a constricted section of the annulus, but the solutions do not converge to the final pure-sedimentation solution with contact from § 5.1. In particular, the limiting solutions with rotation do not trap any pocket. Instead, the constriction has nearly constant radius (see figure 13*c*), and the profile resembles an elastic Landau–Levich or Bretherton-bubble-type configuration (Seiwert, Quéré & Clanet 2013; Warburton *et al.* 2020). Although the approach to the flat centre of the constriction is no longer oscillatory, similar features are seen in elastohydrodynamic line contacts (e.g. Bissett 1989; Bissett & Spence 1989; Lugt & Morales-Espejel 2011; Snoeijer *et al.* 2013).

The key to the scaling observed in figure 13(*b*) is that in the limit $\Omega \to 0$, the dynamics are controlled by the narrow regions at the ends of the constriction. In particular, the thickness of the constriction H becomes controlled by the narrow region at the left-hand end (thinking of θ as a Cartesian coordinate). Here, in view of the relatively small angular scale, (A2) and (5.2) reduce to the Landau–Levich-like equation

$$-\mathcal{B}\Xi^3\Xi''''' \sim Q - \Omega\,\Xi. \tag{A3}$$

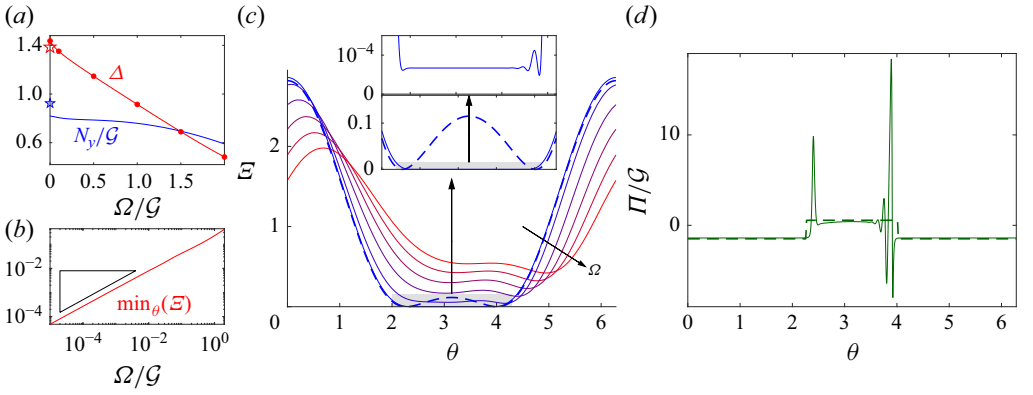

Figure 13. Steady levitated solutions for varying rotation rate Ω, for $(P, \nu, \delta, \mathcal{G}) = (0, 1/2, 1/8, 1/32)$. (*a*,*b*) Plots of Δ, N_y and the minimum gap against $\Omega/\mathcal{G}$. The triangle in (*b*) shows the power law $\Omega^{3/4}$. (*c*) Plot of $\Xi(\theta)$ for the rotation rates shown by the points in (*a*,*b*) (with Ω increasing from blue to red). The inset shows a magnification of the solution with $\Omega = 10^{-5}\mathcal{G}$ around the minimum gap (solid), along with the long-time pure-sedimentation solution also shown in figure 5 (dashed); also shown by the stars in (*a*). (*d*) The corresponding solutions for $\Pi/\mathcal{G}$.

The balance of terms here demands that $Q \sim H\Omega$ and that the angular scale of these regions is $O(H^3\mathcal{B}/\Omega)^{1/5}$. The constant thickness in the centre of the constriction follows because the solution to (A3) converges to $\Xi \sim Q/\Omega$ there. In fact, as we approach the constriction from the left, the far-field solutions to (A3) become exponential; in view of the signs in (A3), two of these exponentials have negative real part, so must be eliminated in order that the solution converges to $\Xi \sim Q/\Omega$. This leaves three boundary conditions to be applied on the left, where the solution to (A3) must be matched to that for the wider gap. This matching demands that the solution grows as a cubic on the left (cf. Warburton *et al.* 2020). That is, $\Xi \sim (\theta - \theta_a)^3$, where $\theta = \theta_a$ again refers to the left-hand edge of the constriction on the original angular scale. But this limiting form demands that the angular scale of the narrow region there must be $O(H^{1/3})$. Hence $O(H^{1/3}) \equiv O(H^3\mathcal{B}/\Omega)^{1/5}$, or $H = O(\Omega/\mathcal{B})^{3/4}$.

References

Balmforth, N.J., Cawthorn, C.J. & Craster, R.V. 2010 Contact in a viscous fluid. Part 2. A compressible fluid and an elastic solid. *J. Fluid Mech.* **646**, 339–361.

Bannwart, A.C., Rodriguez, O.M.H., de Carvalho, C.H.M., Wang, I.S. & Vara, R.M.O. 2004 Flow patterns in heavy crude oil–water flow. *J. Energy Resour. Technol.* **126** (3), 184–189.

Bissett, E.J. 1989 The line contact problem of elastohydrodynamic lubrication – I. Asymptotic structure for low speeds. *Proc. R. Soc. Lond. A: Math. Phys. Sci.* **424** (1867), 393–407.

Bissett, E.J. & Spence, D.A. 1989 The line contact problem of elastohydrodynamic lubrication – II. Numerical solutions of the integrodifferential equations in the transition and exit layers. *Proc. R. Soc. Lond. A: Math. Phys. Sci.* **424** (1867), 409–429.

Brenner, H. 1961 The slow motion of a sphere through a viscous fluid towards a plane surface. *Chem. Engng Sci.* **16** (3–4), 242–251.

Cawthorn, C.J. & Balmforth, N.J. 2010 Contact in a viscous fluid. Part 1. A falling wedge. *J. Fluid Mech.* **646**, 327–338.

Charles, M.E., Govier, G.W. & Hodgson, G.W. 1961 The horizontal pipeline flow of equal density oil–water mixtures. *Can. J. Chem. Engng* **39** (1), 27–36.

Ghosh, S., Mandal, T.K., Das, G. & Das, P.K. 2009 Review of oil water core annular flow. *Renew. Sustainable Energy Rev.* **13** (8), 1957–1965.

Hormozi, S., Wielage-Burchard, K. & Frigaard, I.A. 2011 Entry, start up and stability effects in visco-plastically lubricated pipe flows. *J. Fluid Mech.* **673**, 432–467.

HUANG, R. & SUO, Z. 2002 Wrinkling of a compressed elastic film on a viscous layer. *J. Appl. Phys.* **91** (3), 1135–1142.

HUEN, C.K., FRIGAARD, I.A. & MARTINEZ, D.M. 2007 Experimental studies of multi-layer flows using a visco-plastic lubricant. *J. Non-Newtonian Fluid Mech.* **142** (1–3), 150–161.

JOSEPH, D.D., BAI, R., CHEN, K.P. & RENARDY, Y.Y. 1997 Core–annular flows. *Annu. Rev. Fluid Mech.* **29** (1), 65–90.

JOSEPH, D.D. & RENARDY, Y.Y. 2013*a* *Fundamentals of Two-Fluid Dynamics: Part I: Mathematical Theory and Applications*. Springer Science & Business Media.

JOSEPH, D.D. & RENARDY, Y.Y. 2013*b* *Fundamentals of Two-Fluid Dynamics: Part II: Lubricated Transport, Drops and Miscible Liquids*. Springer Science & Business Media.

KODIO, O., GRIFFITHS, I.M. & VELLA, D. 2017 Lubricated wrinkles: imposed constraints affect the dynamics of wrinkle coarsening. *Phys. Rev. Fluids* **2** (1), 014202.

LIGHTHILL, M.J. 1969 Motion in narrow capillaries from the standpoint of lubrication theory. In *CIBA Foundation Symposium – Circulatory and Respiratory Mass Transport*, pp. 85–104. Wiley Online Library.

LUGT, P.M. & MORALES-ESPEJEL, G.E. 2011 A review of elasto-hydrodynamic lubrication theory. *Tribol. Trans.* **54** (3), 470–496.

MACKENZIE, J., SIREN, E., DANESHI, M., MELNICK, R., TRESKATIS, T., WACHS, A., KIZHAKKEDATHU, J.N. & MARTINEZ, D.M. 2022 Fibre-reinforced biocompatible hydrogel to replace single-use plastic tubing in the clinical setting. *Chem. Engng J.* **428**, 131786.

MCKIBBEN, M.J., GILLIES, R.G. & SHOOK, C.A. 2000 Predicting pressure gradients in heavy oil–water pipelines. *Can. J. Chem. Engng* **78** (4), 752–756.

MOYERS-GONZALEZ, M.A., FRIGAARD, I.A. & NOUAR, C. 2004 Nonlinear stability of a visco-plastically lubricated viscous shear flow. *J. Fluid Mech.* **506**, 117–146.

OOMS, G. & BECKERS, H.L. 1972 The flow of a rigid core surrounded by an annular liquid layer through a horizontal tube. *Appl. Sci. Res.* **26**, 321–334.

OOMS, G. & POESIO, P. 2003 Stationary core–annular flow through a horizontal pipe. *Phys. Rev. E* **68** (6), 066301.

OOMS, G., POURQUIE, M.J.B.M. & BEERENS, J.C. 2013 On the levitation force in horizontal core–annular flow with a large viscosity ratio and small density ratio. *Phys. Fluids* **25** (3), 032102.

OOMS, G., VUIK, C. & POESIO, P. 2007 Core–annular flow through a horizontal pipe: hydrodynamic counterbalancing of buoyancy force on core. *Phys. Fluids* **19** (9), 092103.

RODRIGUEZ, O.M.H., BANNWART, A.C. & DE CARVALHO, C.H.M. 2009 Pressure loss in core-annular flow: modeling, experimental investigation and full-scale experiments. *J. Petrol. Sci. Engng* **65** (1–2), 67–75.

SARMADI, P., HORMOZI, S. & FRIGAARD, I.A. 2017 Triple-layer configuration for stable high-speed lubricated pipeline transport. *Phys. Rev. Fluids* **2** (4), 044302.

SARMADI, P., HORMOZI, S. & FRIGAARD, I.A. 2018 Flow development and interface sculpting in stable lubricated pipeline transport. *J. Non-Newtonian Fluid Mech.* **261**, 60–80.

SEIWERT, J., QUÉRÉ, D. & CLANET, C. 2013 Flexible scraping of viscous fluids. *J. Fluid Mech.* **715**, 424–435.

SKOTHEIM, J.M. & MAHADEVAN, L. 2004 Soft lubrication. *Phys. Rev. Lett.* **92** (24), 245509.

SNOEIJER, J.H., EGGERS, J. & VENNER, C.H. 2013 Similarity theory of lubricated Hertzian contacts. *Phys. Fluids* **25** (10), 101705.

SOTGIA, G., TARTARINI, P. & STALIO, E. 2008 Experimental analysis of flow regimes and pressure drop reduction in oil–water mixtures. *Intl J. Multiphase Flow* **34** (12), 1161–1174.

SUN, J., GUO, L., FU, J., JING, J., YIN, X., LU, Y., ULLMANN, A. & BRAUNER, N. 2022 A new model for viscous oil–water eccentric core annular flow in horizontal pipes. *Intl J. Multiphase Flow* **147**, 103892.

TREFETHEN, L.N. 2000 *Spectral Methods in MATLAB*. *SIAM*.

WARBURTON, K.L.P., HEWITT, D.R. & NEUFELD, J.A. 2020 The elastic Landau–Levich problem on a slope. *J. Fluid Mech.* **883**, A40.

XIE, B., JIANG, F., LIN, H., ZHANG, M., GUI, Z. & XIANG, J. 2023 Review of core annular flow. *Energies* **16** (3), 1496.

YAMAKI, N. 1984 *Elastic Stability of Circular Cylindrical Shells*. Elsevier.